Short Communication

Electrochemical Deposition of ZnO Nanorod Arrays onto a ZnO Seed Layer: Nucleation and Growth Mechanism

M. Romero[1,], R. Henríquez[1], E. A. Dalchiele[2]*

[1] Instituto de Química, Facultad de Ciencias, Pontificia Universidad Católica de Valparaíso, Av. Universidad 330, Curauma, Placilla, Valparaíso, Chile.
[2] Instituto de Física& CINQUIFIMA, Facultad de Ingeniería, Herrera y Reissig 565, C.C. 30, 1100 Montevideo, Uruguay.
[*]E-mail: marioromero290@gmail.com

The nucleation and growth mechanisms for the electrochemical synthesis of ZnO nanorod arrays on two different substrates (i.e., a naked FTO/glass substrate and a ZnO thin film seed layer/FTO/glass substrate) were investigated. This study was based on the analysis and deconvolution of the chronoamperometric transient curves that were obtained during the potentiostatic electrosynthesis of ZnO nanostructures. Using this potentiostatic method and existing theoretical formalism, the nucleation kinetic parameters were determined. Analysis of these results indicated that the presence of a seed layer did not change the nucleation or growth mechanisms and only affected the time constant of each contribution (i.e., 3D instantaneous nucleation with diffusion controlled growth and 3D instantaneous nucleation under charge-transfer control) as well as the associated Faradic charge.

Keywords: Nanorod, electrodeposition, NGM, ZnO.

1. INTRODUCTION

Over the last several years, single crystal ZnO nanowire and nanorod arrays (NRAs) have been developed as important building blocks for a new generation of devices in various technology areas, such as optoelectronics, gas sensing, field emission, piezoelectrics and solar cells [1-4]. The physical properties of the ZnO NRAs (i.e., light management in optoelectronic devices) are strongly affected by their morphological characteristics, such as shape, surface density, size and vertical alignment. Therefore, a synthetic process that provides control of the rod shape, size, orientation, and density is important for controlling the properties and performance of NRAs [5].

Among the different synthetic techniques for ZnO NRAs (i.e., chemical vapour and metal-organic chemical vapour deposition [6-9], vapour-liquid-solid deposition [10], electron beam evaporation [11], pulsed laser deposition [12-13] and spray pyrolysis [14]), electrochemical deposition [5,15-19] has emerged as a promising technique for this purpose. The electrochemical deposition (ED) method has many advantages including a low growth temperature, simple and low cost process without the need for vacuum systems for preparing ZnO nanorods with high crystallinity, being suited for scale-up and good electrical contact between the structures and the substrate [16-21]. However, when electrochemical growth of ZnO NRAs on transparent conducting oxides (TCOs, i.e., ITO and FTO), electrodes and a previously deposited ZnO seed layer are required to precisely control the morphology and aspect ratio of the as-grown ZnO nanostructures [22-24]. These characteristics are important for the application of NRAs in solar cells and light-emitting devices because good control of the morphology of the ZnO NRAs is required to optimize the light management in the sample, and controllable growth of well-aligned ZnO NRAs is also possible [22-24].

Therefore, to gain insight into the morphological differences, the nucleation and growth mechanism (NGM) that governs the electrochemical growth of these ZnO nanostructures must be understood. To the best of our knowledge, very few molecular-level studies of the NGM that is involved in the electrochemical synthesis of ZnO NRAs have been reported [25].

In this study, the NGMs for the electrochemical synthesis of ZnO NRAs on two different substrates (i.e., a naked FTO/glass substrate and a ZnO thin film seed layer/FTO/glass substrate) were investigated. This study was based on the analysis and deconvolution of the chronoamperometric transient curves that were obtained during the potentiostatic electrosynthesis of ZnO nanostructures. The different NGM contributions to the global mechanism are discussed. In addition, the influence of the ZnO seed layer on the NGM was studied.

2. EXPERIMENTAL

The electrodeposition of the ZnO nanostructures was performed on tin oxide doped with fluorine (FTO), which was subjected to a washing protocol to remove any residues from the conductive surface. This protocol initially consisted of washing with bidistilled water followed by acetone and n-propanol; during each wash step, 15 min of sonication was employed to remove any residues on the surface. The seed layer solution was prepared using $0.01 \ mol \cdot L^{-1}$ $Zn(CH_3COO)_2.2H_2O$ in ethanol and was added to the FTO by spin coating at 2000 rpm followed by drying at a temperature of 110 °C for 10 min. This process was repeated 4 times followed by heat treatment at a temperature of 350 ºC for 30 min.

The electrolytic solution was prepared using sodium acetate ($CH_3COONa.3H_2O$, $0.1 \ mol \cdot L^{-1}$) (Merck P.A.), and the Zn precursor was zinc acetate ($Zn \ (CH_3COO^-)_2.2H_2O$, $0.001 \ mol \cdot L^{-1}$) (Merck PA). The pH was maintained at a value of 6.5 using CH_3COOH, and the solutions were prepared in ultrapure water (18.2 MΩ·cm). In addition, the solution was saturated with high purity oxygen for 30 min prior to the electrochemical synthesis and throughout the experiment. The synthesis temperature was adjusted to 70 °C using a thermostat PolyScience model 9106, and the electrochemical measurements were performed using a potentiostat CH Instruments model 604C. The electrosynthesis

of the ZnO nanostructures using potentiostatic techniques was performed (potential step) in a typical three-electrode cell. The working electrodes consisted of glass slides covered with fluor doped tin oxide thin films (FTO, 1 cm^2), and the reduction potential was –1.0 V for 60 min at 70 °C under stirring. The counter electrode sheet, which was supplied by Alfa Aesar, was 99% Zn with a size of 4 cm^2 and a thickness of 1.6 mm, and the reference electrode was a saturated calomel electrode (SCE).

The field emission scanning electron microscopy (FE-SEM) images of the AZO/FTO/glass substrate seed layers and ZnO NRAs were obtained on a Helios Nanolab 650 Dual Beam (FEI Co.). These FE-SEM images were recorded under the following conditions: an operating voltage of 2 kV and a current of 100 pA in Mode II: Immersion through lens detector.

The X-ray diffraction (XRD) measurements were performed using a Philips PW3710 diffractometer with CuK$_\alpha$ radiation in a Bragg-Brentano configuration. The accelerating voltage was set to 40 kV with a 25 mA flux.

3. RESULTS AND DISCUSSION

3.1. Morphological and structural characterization

Figure 1 shows the typical FE-SEM micrograph images of the ZnO nanorod arrays (NRAs) obtained by electrodeposition onto a naked FTO/glass substrate and a ZnO seed layer/FTO/glass transparent electrode substrate. The sample without a seed layer was composed of ZnO nanorods with a diameter of approximately 250-300 nm, and the sample deposited onto the ZnO thin film seed layer exhibited a mean nanorod diameter of 80-90 nm. Moreover, few ZnO NRAs were grown on a naked FTO/glass substrate (nanorod density of ca. $6 \cdot 10^8$ cm^{-2}), and these NRAs were not well aligned. However, the ZnO NRAs that were grown on a ZnO seed layer were dense (nanorod density of ca. $3 \cdot 10^9$ cm^{-2}) and vertically oriented to the substrate plane with the axial direction aligned with the *c*-axis of the hexagonal ZnO crystal structure. The effect of the ZnO seed layer on the final morphology and structure of the electrochemically grown ZnO nanorod arrays has been previously reported [26-27].
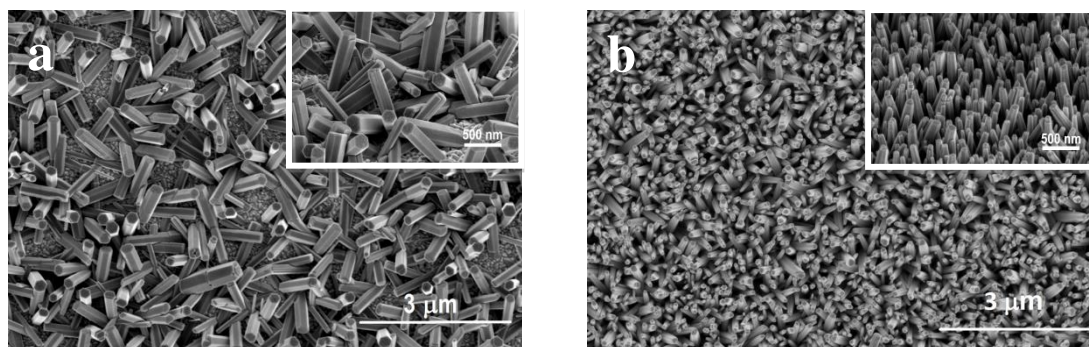

Figure 1. (a) Plan-view FE-SEM micrograph images of ZnO nanorod arrays electrochemically grown on a bare FTO/glass substrate. Inset: high-magnification SEM micrograph view of the same sample and with a tilt angle of 45°. (b) SEM plan-view micrograph image of ZnO nanorod arrays electrochemically grown on a ZnO seed layer/FTO/glass electrode substrate. Inset: high-magnification SEM micrograph view of the same sample and with a tilt angle of 45°.

Figure 2 shows the typical X-ray diffraction patterns for the ZnO NRAs that were obtained by electrodeposition on a naked FTO/glass substrate and a ZnO thin film seed layer as well as the standard reference powder diffraction pattern for hexagonal ZnO. The X-ray diffraction peaks can be indexed to the hexagonal wurtzite ZnO structure (JCPDS file No. 05-0664) and the SnO_2 phase, which originates from the FTO substrate [28]. Seven diffraction peaks corresponding to the (10$\underline{1}$0), (0002), (10$\underline{1}$1), (10$\underline{1}$2), (11$\underline{2}$0), (10$\underline{1}$3) and (11$\underline{2}$2) crystallographic planes of the ZnO hexagonal wurtzite structure were observed in the X-ray diffraction pattern of the ZnO NRAs grown on a bare FTO/glass substrate. The lack of (10$\underline{1}$0) and (10$\underline{1}$1) ZnO diffraction peaks and decrease in intensity of the (0002) ZnO diffraction peak were observed in the X-ray diffraction pattern of the ZnO NRAs grown onto the ZnO seed layer. The intense (0002) ZnO diffraction peak confirmed that the ZnO nanorods were highly crystalline with a hexagonal structure. In addition, the preferential growth of the ZnO NRs was perpendicular to the substrate, which was confirmed by the FE-SEM images shown in Fig. 1. Because the ZnO nanorods were single crystals with the *c*-axis aligned along their longitudinal axis, the crystallographic orientation degree of the samples may indicate the verticality of the nanorods [29]. To characterize this (000l) texture, the $I_{0002}/I_{10\underline{1}1}$ intensity ratio was determined [30-32]. Here, I_{0002} and $I_{10\underline{1}1}$ are the intensities of the (0002) and (10$\underline{1}$1) diffraction lines. The ZnO (10$\underline{1}$1) line was selected because this line is the strongest XRD line for standard ZnO powder with no preferred orientation [31]. The $I_{0002}/I_{10\underline{1}1}$ value from standard ZnO JCPDS values is 0.56 [28]. In this study, the calculated $I_{0002}/I_{10\underline{1}1}$ intensity ratio value was 1.6 and 23.0 for the ZnO NRAs samples grown on a naked and ZnO seed layer substrate, respectively. These results confirm that the characteristics of the ZnO NRAs are well-shaped *c*-axis oriented hexagonal columns, and these characteristics improved due to the use of a ZnO seed layer. The intensity of the (0002) Bragg peak would be stronger for narrower angular distributions along the normal to the substrate.
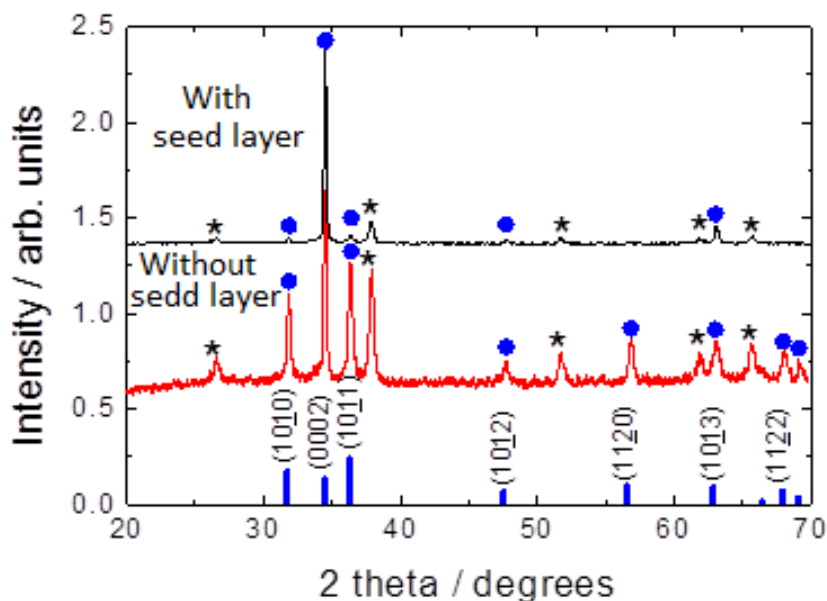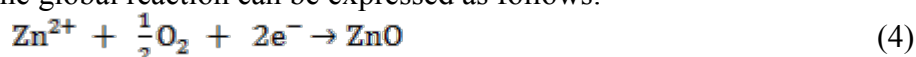

Figure 2. X-ray diffraction patterns of ZnO nanorod array samples that were electrochemically grown on a bare FTO/glass substrate and a ZnO thin film seed layer/FTO/glass substrate. The diffraction planes are indicated for ZnO. The hexagonal wurtzite ZnO JCPDS pattern is also shown for comparison (ZnO JCPDS: thick black bars). (* indicates the peaks originating from the SnO_2:F substrate).

3.2. Nucleation and growth mechanism study

During the electrochemical growth of the ZnO NRAs, different processes are involved including chemical and electrochemical processes. The first electrochemical step is the electroreduction of molecular oxygen in the solution (provided by bubbling oxygen in the solution to saturation) to hydroxide ions in a four-electron reaction. Then, two chemical steps occurred. First, a chemical precipitation occurred, and then, a dehydration step occurred at temperatures higher than 39 °C, which resulted in the formation of the ZnO phase. Our proposed mechanism is as follows [33-34]:

$$O_2 + 2H_2O + 4e^- \rightarrow 4OH^- \tag{1}$$
$$Zn^{2+} + 2OH^- \leftrightarrows Zn(OH)_2 \tag{2}$$
$$Zn(OH)_2 \overset{\Delta}{\rightarrow} ZnO + H_2O \tag{3}$$

Therefore, the global reaction can be expressed as follows:
$$Zn^{2+} + \frac{1}{2}O_2 + 2e^- \rightarrow ZnO \tag{4}$$

To better understand the influence of the ZnO seed layer on the final morphology of the electrochemically grown ZnO nanorod arrays, we studied the nucleation and growth mechanism using a potentiostatic current density-time transient technique. The nucleation kinetics and growth of the first nuclei formed on the initial substrate are critical steps that determine the physicochemical and morphological properties of the electrodeposited materials and must be understood and controlled to achieve the targeted properties [35-36].

Figure 3 shows the experimental potentiostatic current density-time transients for the electrodeposition of ZnO NRAs onto a naked FTO/glass substrate and a ZnO thin film seed layer/FTO/glass substrate at a –1.0 V vs. SCE applied potential value. The shapes of these current density transients are complex and very different from each other, which may indicate the existence of different NGMs depending on the absence or presence of a ZnO seed layer on the FTO/glass substrate. For the naked FTO/glass substrate, after applying the potential step, a maximum (–1.8 mA·cm^{-2}) was reached after the initial increase in the current density (j); then, the current density decayed quickly until it reached an approximately constant value of 0.8 mA·cm^{-2}. For the ZnO thin film seed layer/FTO/glass substrate system, the current density increased sharply after applying the potential step, and a slow current decay was then observed until j reached a nearly constant stationary current density value of ca. –1.0 mA·cm^{-2}. As previously mentioned, the difference in these j-t transients may account for the different ZnO nanostructures, which are shown in Fig. 1. In addition, the differences may be due to different NGMs for both the early and prolonged electrocrystallization stages.

Next, the experimental j/t transients were fitted using a mathematical function that consisted of a sum of two contributions. The best results were obtained with the following global $j(t)$ equation, and the parameters of this equation are summarized in Table 1.

$$j(t) = j(t)_{IN3D_{Diff}} + j(t)_{IN3D_{ct}} \tag{5}$$

where $j(t)_{IN3D_{Diff}}$ and $j(t)_{IN3D_{ct}}$ are the current density contributions corresponding to 3D instantaneous nucleation with diffusion controlled growth and 3D instantaneous nucleation under charge-transfer control, respectively.
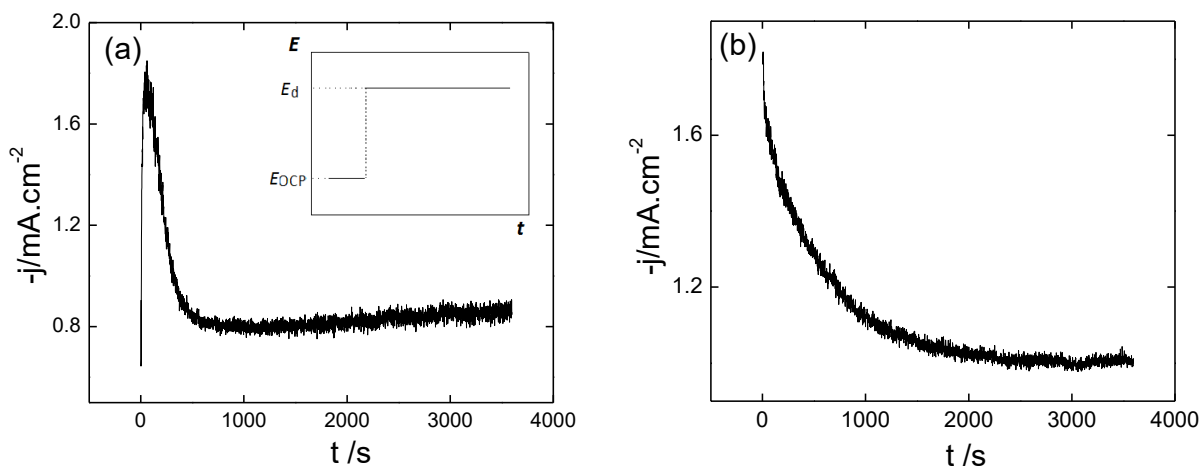

Figure 3. Experimental potentiostatic current density-time transients for ZnO NRAs electrodeposited on (a) a naked FTO/glass substrate and (b) a ZnO thin film seed layer/FTO/glass substrate from an aqueous solution consisting of 0.001 M zinc acetate + 0.1 M sodium acetate. The experimental conditions were as follows: electrolytic bath temperature: 70 °C, pH 6.5, and electrodeposition potential E_d= –1.0 V vs. SCE. The inset of Fig. 3(a) shows the applied E/t potential step program. E_{OCP} is the open circuit potential.

Table 1. Nucleation and Growth Models used to fit the j/t Transients.

Contribution	$j=F(t)$	Parameters[a]	3D centres[b]
IN3D$_{diff}$	$j = P_1 t^{-0.5}[1 - exp(-P_2 t)]$	$P_1 = \dfrac{nFD^{0.5}C^\infty}{\pi^{0.5}}$ $P_2 = N_0\pi\left(\dfrac{8\pi C^\infty M}{\rho}\right)^{0.5}D$	
IN3D$_{tc}$	$j = P_3[1 - exp(-P_4 t^2)]$	$P_3 = nFk_3^{''}$ $P_4 = \dfrac{\pi M^2 k_3^2 N_0}{\rho^2}$	
Global equation	$j(t) = j_{IN3D_{diff}}(t) + j_{IN3D_{ct}}(t)$		

[a] nF is the molar charge transferred during the ZnO electrodeposition process; D, C^∞, M and ρ are the diffusion coefficient, the concentration in the bulk of the solution, the molar mass and the density of the phase, respectively. N_0 is the number density of the active sites for nucleation on the electrode

surface. k_3 and k'_3 are the nuclei three-dimensional growth rate constants perpendicular and parallel to the electrode surface, respectively.

[b] Three-dimensional growth centres: hemispherical and right circular cone.

Figure 4 shows the experimental and nonlinear fitted (with the global eq. 5) j/t transients shown in Fig. 3. The individual contributions from the different processes (i.e., IN3D$_{diff}$ and IN3D$_{tc}$) are also shown in Fig. 4. The fits were very good along the studied time range. Moreover, the P_1, P_2, P_3 and P_4 parameters are shown in Table 2. For the growth of ZnO NRAs on a bare FTO/glass substrate, the NGM consists of two 3D instantaneous nucleation contributions (i.e., diffusion controlled growth charge-transfer controlled growth). In this case, the initial stages of electrocrystallization were largely associated with IN3D$_{diff}$, indicating that growth of the first $Zn(OH)_2$ nuclei (that after heat passes to ZnO) on a bare FTO/glass substrate was limited by molecular oxygen diffusion from the solution bulk to the electrolyte/substrate interface. This leads to the formation of hemispheric nucleation centres, which grow independently of the other centres until they overlap, which explains the presence of the current density maximum observed in Fig. 4. Then, as overlapping progresses, the current density decays, and then, the IN3D$_{tc}$ contribution to the NGM becomes increasingly important. This contribution achieves a stationary state at longer times of the studied time range. This NGM behaviour results in the rate of ion zinc incorporation into the $Zn(OH)_2$ nuclei lattice becoming the determining step of this NGM process.
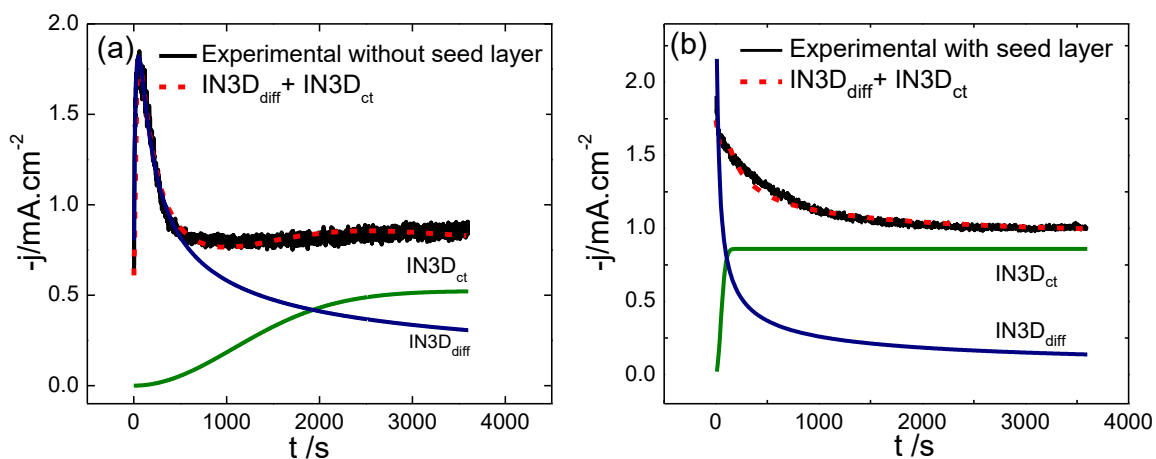

Figure 4. Experimental and fitted j-t transients that were recorded during the electrodeposition of ZnO NRAs on (a) a naked FTO/glass substrate and (b) a ZnO thin film seed layer/FTO/glass substrate from an aqueous solution consisting of 0.001 M zinc acetate + 0.1 M sodium acetate. The experimental conditions were as follows: electrolytic bath temperature: 70 °C, pH 6.5, and electrodeposition potential E_d= −1.0 V vs. SCE. The individual contributions from different processes (i.e., IN3D$_{diff}$ and IN3D$_{tc}$) are also shown.

Then, under this IN3D$_{tc}$ NGM, 3D right circular cone growth centres grow on the previously formed hemispherical ones. Moreover, when these cone growth centres are impeded to grow in a

lateral fashion, these centres can only grow perpendicularly to the substrate surface, resulting in the formation of these ZnO NRAs. For the NGM of a ZnO thin film seed layer/FTO/glass substrate (see Fig. 4b), a similar behaviour can be expected with the same first $IN3D_{diff}$ and second $IN3D_{tc}$ contributions. However, in comparison to the NGM results for a bare FTO/glass substrate, both contributions emerged more quickly. Therefore, for the ZnO NRAs grown on a ZnO thin film seed layer/FTO/glass substrate, the nucleation and coalescence processes occurred more quickly. The coalescence behaviour is indicative of the high density of the starting nuclei. In fact, the higher density of the nuclei on the seeded FTO substrates may be due to the seed layer, which is composed of ZnO nanoparticles [24]. Therefore, these densely packed ZnO nanocrystals may act as homoepitaxial nucleation sites [24]. However, the bare FTO substrate has a high nucleation potential barrier, resulting in a lower density of nucleation sites [24]. Moreover, the short time required to reach coalescence suggests that the nuclei did not grow very large before the nanostructure growth stage, which gives rise to ZnO NRAs with smaller and homogeneous diameters, as shown in Fig. 1. For the NGM study on a bare FTO substrate, a second $IN3D_{tc}$ contribution appeared at shorter times, as discussed above.

Table 2. Parameters obtained by Nonlinear Fitting of Equation 5 to the Experimental Potentiostatic Current Density-Time Transients shown in Figure 4.

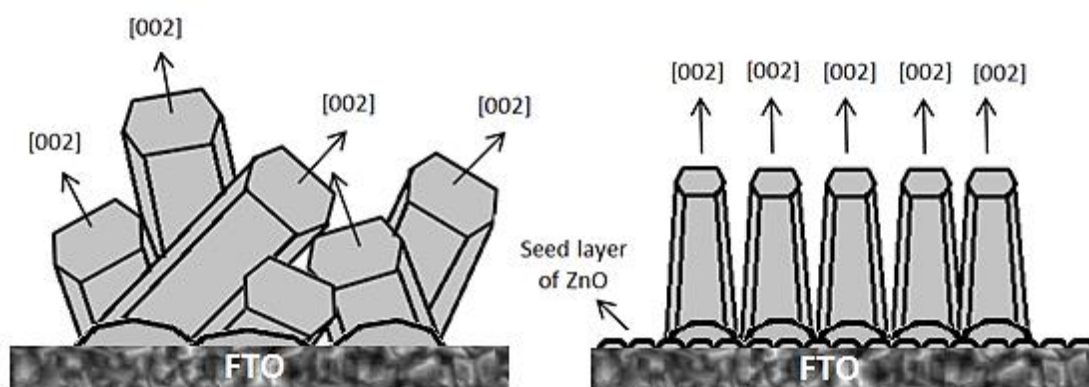| Substrate	P_1 (A·s$^{1/2}$·cm^{-2})	P_2 (s^{-2})	P_3 (A·cm^{-3})	P_4 (s^{-3})
Naked FTO/glass	18.39	0.024	0.522	4.3×10^{-7}
ZnO thin film seed layer/FTO/glass	8.22	0.968	0.860	2.3×10^{-4}

Table 3. Comparison of the Associated Charges for Each Contributions to the NGM obtained on a Bare FTO/Glass Substrate and a ZnO Thin Film Seed Layer/FTO/Glass Substrate.

NGM contribution	% Faradaic charge	
	Without ZnO seed layer	With ZnO seed layer
$IN3D_{diff}$	62.8	23.7
$IN3D_{ct}$	37.2	76.3

Table 3 shows the Faradaic charges associated with each contribution in the presence or absence of a ZnO seed layer. In the absence of the seed layer, the $IN3D_{diff}$ process contributes a minor amount compared to that contributed by the $IN3D_{ct}$ one, indicating its greater contribution and importance to the global growth process. However, the opposite behaviour was observed when the initial substrate contains a seed layer on its surface. The observed change can be associated with the energy of the pre-existing ZnO nuclei on the surface of the electrode that guide the preferential growth on the substrate. Based on these values and as shown in Fig. 4, both processes appeared at shorter times when a ZnO seed layer electrode was employed. According to the FE-SEM images (see Fig. 1), the highest charge associated with the $IN3D_{ct}$ process coupled with its rapid development results in the

formation of nanorods with a smaller diameter that have a more uniform nanorod diameter distribution with a significant increase in their surface area.

These results are also consistent with the observations obtained from the X-ray diffraction patterns, which indicated a preferred crystallographic orientation in the (0002) plane. Scheme 1 shows the growth of the ZnO nanorods on bare FTO and ZnO thin film seed layer/FTO/glass substrates, respectively. In the first case, three-dimensional nuclei that are controlled by diffusion are formed. Due to their large size, these nuclei favour coalescence of the three-dimensional growth centres, which is controlled by charge transfer (resulting in the circular cone shape that is characteristic of the IN3D$_{ct}$). Therefore, a disordered deposit without a preferential texture was obtained. In the presence of a seed layer, the pre-existing ZnO nuclei assisted the perpendicular growth of the ZnO nanorods, and the hemispherical nuclei that were formed by the diffusion process do not introduce significant distortion in the orientation of the final deposit.

Scheme 1. Representation of the growth of ZnO nanorods onto a naked FTO/glass substrate and a ZnO thin film seed layer/FTO/glass substrate.

Based on the P_2 parameter values that are reported in Table 2 and the mathematical expression tabulated in Table 1, the number density of the active sites for nucleation on the electrode surface (N_0) was determined. N_0 values of $6 \cdot 10^4$ cm^{-2} and $1 \cdot 10^8$ cm^{-2} were obtained for the naked FTO/glass substrate and ZnO thin film seed layer/FTO/glass substrate, respectively. However, these experimentally determined N_0 values were much smaller than that obtained from the FE-SEM analysis (see above). This discrepancy may be due to neglecting the effect of the nucleus size, substrate interaction, and substrate cleanliness [27-38].

Based on the P_1 parameter values reported in Table 2 and the mathematical expression tabulated in Table 1, the diffusion coefficient (D) for molecular oxygen in the electrolytic bath of the two studied systems (i.e., a naked FTO/glass substrate and a ZnO thin film seed layer/FTO/glass substrate as the electrodes) was determined. The obtained D values were $2.9 \cdot 10^{-5}$ cm$^2 \cdot$s^{-1} and $5.71 \cdot 10^{-6}$ cm$^2 \cdot$s^{-1} for the naked FTO/glass substrate and the ZnO thin film seed layer/FTO/glass substrate electrodes, respectively. These values are similar to those previously reported ($4.63 \cdot 10^{-5}$ cm$^2 \cdot$s^{-1} at 70.3 °C) [39].

4. CONCLUSIONS

In this study, the effect of the seed layer on the NGM of the ZnO nanorods was studied. The results indicate that the presence of a seed layer does not change the nucleation and growth mechanisms. Only the time constant of each contribution involved ($IN3D_{diff}$ and $IN3D_{ct}$) as well as the associated Faradic charge were affected. The potentiostatic electrodeposition of ZnO nanorods onto a FTO/seed layer surface led to the formation of more ordered and textured nanostructures that were characterized by a smaller diameter nanorod and high transparency compared to that on a clean FTO substrate. These results were confirmed by the FE-SEM images and XRD patterns, which indicated the presence of a single-phase hexagonal wurtzite-type phase. The XRD patterns contained an intense peak that corresponded to the (002) plane, which is favoured when amending FTO with a seed layer of the same compound.

References

1. Y. Hames, Z. Alpaslam, A. Kösemen, S.E. San, Y. Yerli, *Sol Energy.* 84 (2010) 426.
2. B. Kumar, S.W. Kim, *Nano Energy.* 1 (2012) 342.
3. R. Tena-Zaera, J. Elias, G. Wang, C. Lévy-Clément, *J Phys Chem C.* 111 (2007) 16706.
4. M. Seol, H. Kim, Y. Tak, K. Yong, *Chem Commun.* 46 (2010) 5521.
5. Th. Pauporté, G. Bataille, L. Joulaud, F.J. Vermersch, *J Phys Chem C.* 114 (2010) 194.
6. M. Seol, H. Kim, Y. Tak, K. Yong, *Chem. Commun,* 46 (2010) 5521.
7. B. Kumar, S.W. Kim, *Nano Energy.* 1 (2012) 342.
8. Y. Chen, L. Wei, G. Zhang, J. Jiao, *Nanoscale Research Letters.* **7** (2012) 516.
9. Y. Tak, S.J. Hong, J.S. Lee, K. Yong, *J Mater Chem.* 19 (2009) 5945.
10. M. Huang, S. Mao, H. Feick, H. Yan, H. Kind, E. Weber, R. Russo, P. Yang, *Science.* 292 (2001) 1897.
11. D.J. Qiu, P. Yu, H.Z. Wu, *Solid State Commun.* 134 (2005) 735.
12. M.A. Susner, S.D. Carnevale, T.F. Kent, L.M. Gerber, P.J. Phillips, M.D. Sumption, R.C. Myers, *Phys. E.* 62 (2014) 95.
13. S. Thanka Rajan, B. Subramanian, A.K. Nanda Kumar, M. Jayachandran, M.S. Ramachandra Rao, *J of Alloys and Compounds* 584 (2014) 611.
14. A. Maldonado, R. Asomoza, J. Cañetas-Ortega, E.P. Zironi, R. Hernández, R. Patiño, O. Solorza-Feria, *Sol Energy Mater Sol Cells.* 57 (1999) 331.
15. M. Guo, C.Y. Yang, M. Zhang, Y. Zhang, T. Ma, X. Wang, *Electrochim Acta.* 53 (2008) 4633.
16. Th. Pauporté, *Lecture Notes in Nanoscale Sci Technol.* 5 (2009) 77.
17. D. Lincot, *MRS Bulletin.* 35 (2010) 778.
18. C.D. Bojorge, V.R. Kent, E. Teliz, H.R. Cánepa, R. Henríquez, H. Gómez, R.E. Marotti, E.A. Dalchiele, *Phys Status Solidi A.* 208 (2011) 1662.
19. G. Guerguerian, F. Elhordoy, C.J. Pereyra, R.E. Marotti, F. Martín, D. Leinen, J.R. Ramos-Barrado, E.A. Dalchiele, *Nanotechnology.* 22 (2011) 505401.
20. H. Kim, J.Y. Moon, H.S. Lee, *Electron Mater Lett.* 7 (2011) 59.

21.   M.R. Khajavi, D.J. Blackwood, G. Cabanero, R. Tena-Zaera, *Electrochim Acta* 69 (2012) 181.
22. G. Kenanakis, D. Vernardou, E. Koudoumas, N. Katsarakis, *J Cryst Growth*. 311 (2009) 4799.
23. C. Lévy-Clément, J. Elias, *ChemPhysChem*. 14 (2013) 2321.
24. L. Campo, E. Navarrete-Astorga, C.J. Pereyra, A. Cuevas, R. Romero, D. Ariosa, R. Henríquez, E. Muñoz, R.E. Marotti, F. Martín, J.R. Ramos-Barrado, E.A. Dalchiele. The effect of a sputtered Al-doped ZnO seed layer on the morphological, structural and optical properties of electrochemically grown ZnO nanorod arrays. *In press to Journal of the Electrochemical Society*. (2016).
25. S. Xu, Z.L. Wang, *Nano Research*. 4 (2011) 1013.
26. J. Song, S. Lim, *J Phys Chem*. 111 (2007) 596.
27. D.Y. Song, K.H. Bae, H.S. Kim, N.K. Park, *J Phys Chem C*. 119 (2015) 10321.
28. Powder Diffraction File, Joint Committee for Powder Diffraction Studies (JCPDS) File No. 05-0664 (hexagonal structure of ZnO), 1999.
29. J. Elias, R. Tena-Zaera, C. Lévy-Clément, *Thin Solid Films* 515 (2007) 8553.
30. M. Rusu, G.G. Rusu, M. Girtan, S. DabosSeignon , *J Non-Cryst Solids*. 354 (2008) 4461.
31. S. Mondal, K. Prasad, P. Mitra, *Materials Research*. 16 (2013) 94.
32. S.V. Thach, M. Jouan, S.N. Xuan, T.N. Hoang, H.P. Pham, *Physics and Engineering of New Materials Springer Proceedings in Physics* 127 (2009) 171.
33. G. Jiangfeng, D. Zhaoming, D. Qingping, X. Yuan, Z. Weihua, *Nanomater*. 2010 Article ID740628.
34. L. Liang, P. Shusheng, D. Xincun, Z. Yonggang, H. Xiaohu, Y. Youwen, L. Guanghai, Z. Lide, *J Phys Chem C*. 111 (2007) 7288.
35. M. Paunovic, M. Schlesinger in: Fundamentals of Electrochemical Depositions, (1998), Wiley-Interscience, New York.
36. S. Bijani, R. Schrebler, E.A. Dalchiele, M. Gabás, L. Martínez, J.R. Ramos-Barrado, *J Phys Chem C*. 115 (2011) 21373.
37. R.K. Pandey, S.N. Sahu, S. Chandra Handbook of semiconductor electrodeposition, (1996), Marcel Dekker, Inc; USA.
38. J.W.M. Jacobs. *J Electroanal Chem*. (1988) 135
39. P. Han, D.M. Bartel, *J. Phys. Chem*. 100 (1996) 5597.